Peer-reviewed version available at *Catalysts* **2018**, *8*, 454; doi:10.3390/catal8100454

Article

Hydrogen oxidation on Ni-based electrocatalysts: the effect of metal doping

Elena S. Davydova[1,2,*], **Jérémie Zaffran**[2,3], **Kapil Dhaka**[3], **Maytal Caspary Toroker**[2,3,*], **Dario R. Dekel**[1,2,*]

[1] The Wolfson Chemical Engineering Department, Technion – Israel Institute of Technology, 3200003 Haifa, Israel,
[2] The Nancy and Stephen Grand Technion Energy Program (GTEP), Technion – Israel Institute of Technology, 3200003 Haifa, Israel,
[3] Department of Material Science and Engineering, Technion – Israel Institute of Technology, 3200003 Haifa, Israel,
* Correspondence: elena.s.davydova@gmail.com [E.S.D.], maytalc@technion.ac.il [M.C.T.], dario@technion.ac.il [D.R.D.]. Tel.: +972-54-9958377 [E.S.D].

Abstract: Carbon supported nanoparticles of monometallic Ni catalyst and binary Ni-Transition Metal (Ni-TM/C) electrocatalytic composites were synthesized via chemical reduction method, where TM stands for the doping elements Fe, Co, and Cu. The chemical composition, structure and morphology of the Ni-TM/C materials were characterized by X-ray photoelectron spectroscopy (XPS), X-ray diffractometry (XRD), transmission electron microscopy (TEM), scanning transmission electron microscopy (STEM) and energy-dispersive X-ray spectroscopy (EDS). The electrochemical properties towards hydrogen oxidation reaction in alkaline medium were studied using the rotating disc electrode and cycling voltammetry methods. A significant role of the TM dopant in the promotion of the hydrogen electrooxidation kinetics of the binary Ni-TM/C materials were revealed. A record-high in exchange current density value of 0.060 mA cm^2_{Ni} was measured for Ni_3Fe_1/C, whereas the monometallic Ni/C counterpart has only shown 0.039 mA cm^2_{Ni}. In order to predict the feasibility of the electrocatalysts for hydrogen chemisorption, density functional theory was applied to calculate the hydrogen binding energy and hydroxide binding energy values for bare Ni and Ni_3TM_1.

Keywords: metal doping, nickel-based catalyst, transition metals, synthesis, hydrogen oxidation reaction, exchange current density, alkaline medium, DFT, hydrogen binding energy, hydroxide binding energy.

1. Introduction

Anion exchange membrane fuel cells (AEMFCs) have seen a rapid increase in interest in recent years [1,2], as they promise to overcome the existing cost barriers inherent to low temperature acidic polymer electrolyte membrane fuel cells. In the past 3 years, extensive research in AEMFCs, mainly in polymer performance stability [3–12], carbonation effects [13–15] and modelling [16–19], led to significant progress in this technology. However, in spite of this progress, in order to fulfill the optimistic potential of AEMFCs in the near future, catalysts should be completely free of expensive noble metals, and eventually free of critical raw materials. Although great progress has been done in the development of Pt-free catalysts for oxygen reduction reaction in base medium [20,21], significantly less attention has been paid to the catalysis for the hydrogen oxidation reaction (HOR). The lack of fundamental understanding of the HOR mechanism in basic media and of the main energy barriers needs to be firmly established to overcome this challenge. In a recently comprehensive study, challenges of HOR catalysis in alkaline electrolytes were recently reviewed

Peer-reviewed version available at *Catalysts* **2018**, *8*, 454; doi:10.3390/catal8100454

[22]. The review presents the most updated understanding of the HOR electrocatalysis in basic media and outlines promising future research directions for the development of better HOR electrocatalysts for alkaline electrolytes, mainly to be used for advanced AEMFC devices.

High-performance AEMFCs have been recently reported, showing peak power values that well exceed 1.0 W cm^{-2}; predicting performance stability in anion exchange membrane fuel cells [7,23] however, all of these state-of-the-art AEMFCs exclusively rely on Pt-based HOR catalysts [24]. Very few studies reporting AEMFC performance with zero-platinum loading can be found [24]. Among them, the highest performing Pt-free AEMFCs consist of palladium-based catalysts for the HOR, showing performance close to that of platinum, with peak power densities of 0.4-1.4 W cm^{-2} [25–27]. However, complete removal of platinum group metals (PGMs) in AEMFC anodes is still widely recognized as a major challenge [22,24].

Nickel exhibits the most promising HOR activity of any of the 3d transition metals (TM) [22]. However, until now, undoped Ni electrocatalysts demonstrate about two orders of magnitude lower activity than Pt or Pd [22]. Calculations predicted that doping of Ni by TMs decreases Ni-H bond strength [28,29], thus, allowing to optimize hydrogen binding energy (HBE) values via positively shifting them close to those of PGMs [30]. Nickel doping was also reported to suppress nickel oxophilicity, and hence, to impede surface (electro)oxidation [31]. It was reported that alloying Ni with other 3d TM helps to prevent the formation of Ni-hydride and increases the durability of the electrodes in HER [32,33], strengthening the understanding that Ni doping is a powerful tool in modifying and tailoring Ni (electro)catalytic properties.

Several studies have examined the doping effect of TM for some binary [29,34–38] and ternary [29] Ni-based alloys for HOR in base media. Sheng et al. [29] shown that ternary metallic CoNiMo layers electrodeposited on the surface of Au substrate exhibit a significant increase of exchange current density (0.015 mA cm^{-2}), as compared to bulk Ni (0.002 mA cm^{-2}). The authors suggested that the formation of multi-metallic bonds modified the HBE value of Ni and likely contributed to the enhanced HOR activity [29]. However, thick layers of the electrodeposited CoNiMo layers might be of low practical interest for real AEMFC devices. Kabir et al. [34] developed 50% Ni_9Mo_1/Ketjenblack via thermal reduction method under H_2 flow at 550 °C, with oxidative treatment in 2% O_2/He mixture for 8 h at room temperature. The resultant Ni-Mo catalyst was shown to comprise only ca. 2% $NiMo_4$ alloy, however the authors assumed that the enhanced activity of Ni-Mo catalyst could be ascribed to the decrease in HBE value by ca. 0.14 eV, as compared to that of unmodified Ni. The authors showed that an AEMFC based on this Ni-Mo/C anode catalyst and Pd/C cathode catalyst, can reach a peak power density value of 0.12 W cm^{-2} [34].

In another study, binary Ni-Ag bulk alloys across a range of compositions were deposited on glassy carbon substrate using electron beam evaporation [36]. XRD data showed that e-beam evaporation results only in partial alloying of Ni and Ag, while the rotating disk electrode (RDE) measurements revealed a negligible effect of silver doping on the catalytic activity of Ni towards hydrogen electrooxidation. Zhuang et al. [28] showed that by developing nickel nanoparticles supported on nitrogen-doped carbon nanotubes (CNTs) via hydrothermal treatment at 150 °C in the presence of ammonia and hydrazine, the catalytic activity of bare Ni can be significantly improved (0.028 for Ni/N-CNT vs. 0.0014 mA cm^{-2}_{Ni} for bare Ni in 0.1 M KOH). The authors attributed the promoted HOR activity to the synergetic effect of the optimal HBE resulting both from geometric and electronic interaction of Ni atoms with the edge N atoms in CNT. Although the authors achieved a high mass activity (*ca.* 9 A g_{cat}^{-1}), the elegant but still single data point does not anticipate the future directions for improving the catalytic activity of Ni. Cherstiouk et al. [37] have proposed a series of Ni_xCu_{1-x}/Vulcan XC72 electrocatalysts obtained via successive wet impregnation, calcination and reduction in H_2 at 250 °C for 1 h. The authors assume that the enlargement of the lattice parameter for $Ni_{9.5}Cu_{0.5}$/Vulcan XC72 suggests the formation of Ni-Cu alloy with ca. 5 at.% Cu content. The enhancement of the HOR activity of Ni-Cu samples (0.014 mA cm^{-2}) compared to Ni (0.004 mA cm^{-2}) was tentatively explained by the electronic effect of Cu resulting in the decrease of the energy of adsorption of the hydrogen intermediate.

In summary, certain moderate progress was done in understanding the role of the TM dopant nature and doping level on the catalytic properties of Ni towards HOR in alkaline. However, there is still an enormous gap between systematic understanding of the dopant role in the HOR electrocatalysis and the random data of the experimental data.

In this work, we undertake a systematic scanning of the first row TMs, from Sc to Zn, to predict by density functional theory (DFT) calculations the HBE and OHBE values for three different facets - (111), (200) and (220) - of bimetallic face-centered cubic (FCC) Ni_3TM_1 alloys. To reveal the effect of doping of TM on the electrocatalytic properties of nanosized Ni_3TM_1 electrocatalysts, the HOR kinetics of monometallic Ni/C and bimetallic Ni_3TM_1/C composites in 1 M KOH was also systematically measured for selected TMs that were find potentially interesting by the DFT calculations.

2. Results and Discussion

2.1. Theoretical prediction

DFT was used to calculate the HBE and OH binding energy (OHBE) values on (111), (200), and (220) facets of Ni_3TM_1 alloys. To the best of our knowledge, this is the first time the OHBE values were calculated for electrocatalysts. Figure 1 shows the calculated HBE values (a) and OHBE values (b) for the case of pure Ni and different Ni_3TM_1 alloys. As seen in Figure 1 and Tables A1-A3, hydrogen atom has the lowest HBE for the (111) facet, compared to the (220) and (200) facets. For example, HBE value for bare Ni (111) is -0.54 eV, while is -0.48 and -0.45 eV for Ni (200) and Ni (220), respectively (see also Tables S1-S3, Supporting Information). The reason for the stability of the (111) facet is that H atoms can establish more bonds on (111) facet, which is more atomically dense than other facets. The facet Ni (200) of the bare Ni shows the highest affinity to OH chemisorption and the facet (220) is characterized by the weakest OH bonding (OHBE: (200) << (111) < (220)) (Figure 1, b). The comparison of OHBE and HBE values (HBE and OHBE are -0.54 eV for (111), and HBE is -0.45 and OHBE is -0.49 eV for (220)) shows that the co-adsorption of the both H and OH species is thermodynamically favorable.

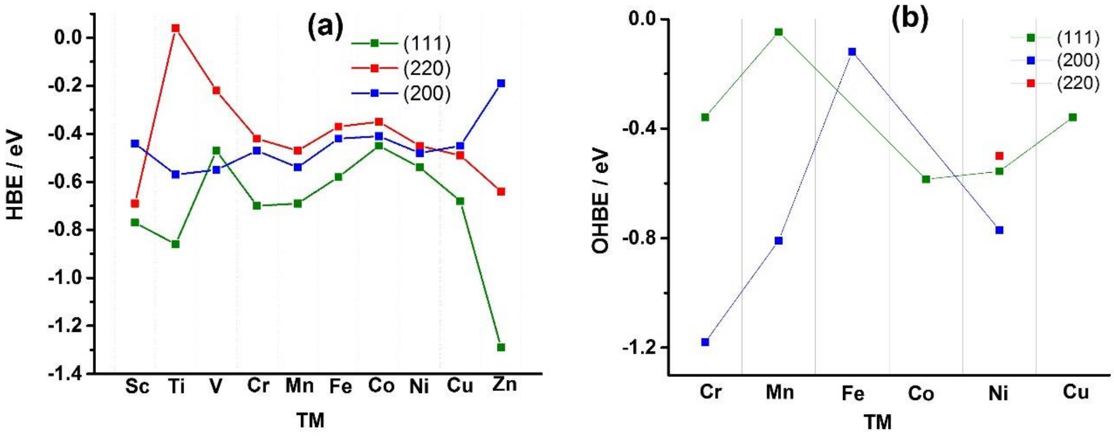

Figure 1. HBE (a) and OHBE (b) values on different facets for Ni_3TM_1 alloys presented in the same order as the 3d TMs in the Periodic Table.

Some authors assume that the kinetics of HOR directly follows the thermodynamics of the reaction [39,40], and therefore it is explicitly related to the HBE values according to the so-called volcano plot [41], where HOR/HER exchange current densities are plotted versus HBE, with the PGMs are normally at the top of the graph. The optimal HBE value was predicted to be ca. -0.24 eV, which corresponds to the HOR $\Delta G \sim 0$ [41]. HBE might be considered as the main factor influencing the HOR kinetics solely in case if the rate-determining step (rds) of the reaction is either Volmer [42], or Heyrovsky reactions [43], namely the removal of the adsorbed H atom from the catalyst surface. Studies of the HOR mechanism in alkaline for Pt electrocatalysts have revealed a controversy in the

Peer-reviewed version available at Catalysts 2018, 8, 454; doi:10.3390/catal8100454

experimental data interpretation [22]: while some of the authors experimentally proved that Tafel reaction is the HOR rds [44–48], others provided experimental evidence for the HOR kinetics limited by the Volmer reaction [49,50].

The mechanism of HOR on Ni-based materials was hardly explored [22,51]. The analysis below is done provided that Volmer or Heyrosky reactions are rds of HOR in alkaline media – the speculative assumption based on the nonlinear dependence of the HOR kinetics on the surface coverage [34,52]. The HBE value calculated for the facet Ni (111), -0.54 eV (Figure 1), is more negative than those calculated for Pt (111), Rh (111) and Ir (111), -0.37, -0.33 and -0.24 eV [30], respectively. In turn, Pt, Rh and Ir show the highest catalytic activity in HOR in alkaline media, which is more than two orders of magnitude higher than that of Ni electrocatalysts [22]. Thus, based on the predicted optimal HBE value [41] and on the calculated HBE values for the most active catalytic materials [22], the recommended HBE values for the newly designed electrocatalysts should fall into the range between ca. -0.33 to -0.24 eV. In case of Ni-based materials, higher catalytic activity would be expected at HBE values which are less negative that those for the bare Ni surfaces.

Among the facets, Pt (100) surpasses the activity of (110) by an order of magnitude, while (111) shows the lowest activity: (110) ≫ (100) > (111) [44,53]. This sequence could be correlated with the HBE values estimated from the peak potential values for the desorption of the underpotentially deposited hydrogen atom in 0.1 M KOH: -0.48 eV for Pt (110) is much less negative compared to -0.60 eV for Pt (100) [39,49]. The exchange current density values, i_0, of carbon supported polycrystalline Pt nanoparticles, Pt/C, and bulk polycrystalline Pt , Pt(pc), are close between each other [54,55] and to i_0 for Pt (110) [44]. Thus, the catalytic activity in HOR might be mainly determined by the presence of the facet Pt (110). The calculations of the HBE values done for Pt(pc) show a span within the range of -0.46 [29] and -0.33 [41] eV, while the value of -0.48 eV is reported for Pt/C [56]. Similar order of activity (Ni (110) > Ni (100) > Ni (111)) is observed in the study of Floner et al. [51]: Ni (100) and above all (110) are the most active than polycrystalline Ni, whereas the behavior of the latter is close to (111), particularly at low pH where dissolution of Ni occurs. Based on the results of Floner et al.[51], we assume that i_0 of the polycrystalline Ni_3TM_1/C electrocatalysts might be dominated by the facet Ni (110) or Ni (220). Interestingly, our calculated HBE values for the bare Ni facets is mostly ordered according to Ni (220) > Ni (200) > Ni (111) (see Figure 1), in good agreement with the activity order experimentally shown by Floner et al. [51]. Furthermore, as seen in Figure 1, it follows that solely alloying Ni with Co results in a positive shift of the HBE value compared to the bare Ni (111) facet, -0.45 vs. -0.54 eV. For the facet (200), the alloying with Sc, Cr, Fe, Co, Cu and Zn were shown to have a positive effect on the HBE values, with only Ni_3Zn_1 (-0.19 eV) close to the aimed range of -0.33÷-0.24 eV. Ni_3Fe_1, Ni_3Co_1 and Ni_3Cu_1 demonstrate the HBE values close to the earlier reported Ni_3Ag_1 [36], CoNi/Mo (110) [29], and Ni/N-CNT [28], the last two materials showing the highest mass specific/surface specific activity values published till now. As regarding the facet (220), the HBE value of Ni_3V_1 falls into the recommended range, and the catalyst might be of interest of the HOR. Ni_3Fe_1 (-0.37 eV) and Ni_3Co_1 (-0.35 eV) of the facet (220) could also result in better HOR than bare Ni catalyst, and therefore, they are included in our experimental work for further study. Thus, based on the theoretical predictions (Figure 1), a series of carbon supported binary electrocatalysts (Ni_3Fe_1, Ni_3Co_1 and Ni_3Cu_1) and monometallic Ni (as reference material) were synthesized by chemical reduction method. Fe, Co and Cu were chosen as the TM dopants due to their promising HBE and OHBE values (Tables A4-A6).

2.2. Physical and chemical characterization

TEM image (Figure S1, a, Supporting Information) shows that electrocatalysts are characterized by nanoscopically uniform distribution of near-spherical particles with the average diameter of ca. 10 nm (Figure S1, b, Supporting Information), surrounded by amorphous carbon support. Assuming spherical particles, the calculated specific surface area of ca. 70 $m^2\ g^{-1}_{Ni}$ would be expected for a particle average diameter of 10 nm.

For binary Ni_3TM_1/C catalysts, element mapping revealed nanoscopically non-homogeneous co-distribution of the metallic components (Figure S2-S4, Supporting Information). This shows that

Peer-reviewed version available at *Catalysts* **2018**, *8*, 454; doi:10.3390/catal8100454

chemical reduction method most likely might result in the formation of composite materials (mechanical mixtures), rather than alloys. The most significant heterogeneity was observed for Ni_3Cu_1/C catalyst (Figure S4, Supporting Information), where separate areas of Ni (red pixels) and Cu (green pixels) can be seen. Surface enrichment by Ni phase (red pixels) was revealed for all the binary Ni_3TM_1/C systems (Figure S2-S4, Supporting Information), which is in good agreement with the XPS data (Table S1, Supporting Information). The opposite – bulk segregation of Ni – was observes in binary Ni_9Mo_1/C electrocatalyst [34]. These observations illustrate that special controlled synthetic approaches are needed in order to synthesize NiTM materials with the given Ni-to-TM ratio. Nevertheless, quite homogeneous metal co-distribution topography was observed for the Ni-Fe and Ni-Co couples in Ni_3Fe_1/C (Figure S2, Supporting Information) and Ni_3Co_1/C (Figure S3, Supporting Information) catalyst, respectively. This latter observation might be related to the fact that Ni co-deposits simultaneously with Co and Fe due to the reduction potential values. To compare, the standard reduction potentials of Ni ($E^0_{Ni^{2+}/Ni^0} = -0.25\,V$) and Co ($E^0_{Co^{2+}/Co^0} = -0.28\,V$) are close, whereas Cu has much higher potential ($E^0_{Cu/Cu^0} = +0.34\,V$). Consequently, the coexistence of the composites with the alloyed phase(s) in Ni_3TM_1/C catalysts cannot be ruled out unambiguously. Therefore, a thorough analysis of the XRD spectra of the as-synthesized catalysts and of those after the thermal treatment at 450 °C was done (Figures S5-S6, Supporting Information). On XRD spectra (Figure S5), catalysts show wide peaks at ~44.5° of low intensity, which correspond to Ni (111) facets, same facet as calculated by DFT (see previous section). Small particle sizes explain the broadening of the (111) peak (with extremely low crystallite sizes of ca. 0.7 nm) and the absence of (200) and (220) reflections on the XRD spectra, which is though does not rule out the coexistence of the high-index facets in the catalysts. The Ni (200) and Ni (220) facets are expected to appear at 51.85 and 76.37°, respectively. All the catalysts are characterized by the presence of hydrated nickel hydroxide $Ni(OH)_2 \times 0.75H_2O$ (#00-038-0715) or nickel oxyhydroxide $Ni_5O(OH)_9$ (#00-027-0340) phase. These phases can be ascribed to the surface oxidation of the catalysts, which potentially may block the electrochemically active surface (see the section below). According to the XPS analysis (Figure S8, Supporting Information), the surface of Ni is predominantly oxidized to NiO, Ni_2O_3 and $Ni(OH)_2$ with the ratio of metallic Ni between 4.5 to 18 at.% (Table S3, Supporting Information). Copper phase in Ni_3Cu_1/C is partially oxidized forming Cu_2O (#00-005-0667), which is in agreement with the XPS data (Figure S7, A, Supporting Information). The crystallite sizes of metallic copper are ca. 22 nm, which is comparable to the catalyst particle sizes (Figure S1, Supporting Information). Shale-up satellites of copper for Ni_3Cu_1/C catalyst (Figure S7, a, Supporting Information) are characteristic to divalent Cu, whereas monovalent Cu has no satellites [57]. The peak at 953.0 can correspond to all three components: zerovalent Cu (Cu $2p_{1/2}$ at 952.6 eV) [58], monovalent (Cu $2p_{1/2}$ at 952.7 eV) [59] or divalent Cu (Cu $2p_{1/2}$ at 952.5 eV) [60], as well as the peak at ca. 933 eV. High resolution XPS spectrum for Ni_3Fe_1/C (Figure S7, b) shows three distinguishable peaks: a peak of the highest intensity at binding energy (BE) ~712÷714 eV which could be ascribed to Fe^{3+} salts, but most probably arises from Ni LMM Auger peak (712 eV), overlapping with Fe $2p_{3/2}$. Peak of low intensity at 707.9 eV corresponds to metallic Fe [61]. The broad peak at ca. 725 eV can be ascribed to either Fe_2O_3 (Fe $2p_{1/2}$ at 724 eV) [62], or FeOOH (Fe $2p_{1/2}$ at 724.3 eV) [62], or Fe_3O_4 (Fe $2p_{1/2}$ at 723.5 eV) [62]. It is more challenging to determine the concentration and chemical shifts of cobalt for Ni_3Co_1/C CR-synthesized catalyst, since Co $2p_{3/2}$ is close to Ni LMM structure and Co 3p spectrum overlaps with the one for Ni 3p.

The XRD spectra registered on the as-synthesized Ni_3TM_1/C catalysts cannot provide a clear evidence of metal alloying. Therefore, thermal treatment at 450 °C in reducing atmosphere was used as an indirect indication of the presence of several metallic phases in the as-synthesized materials. The XRD spectra deconvolution for the heat-treated Ni_3Fe_1/C (Figure S6, d) and Ni_3Cu_1/C (Figure S6, c) have shown a splitting of the reflections into two peaks. One of them can be ascribed to the alloy phases enriched by Ni and by the other – to the second transition metal. For instance, the reflections of Ni_3Cu_1/C at the angles of 44.16, 51.45 and 75.92 are close to those for the alloy Ni_3Cu_1 (#04-004-4502), whereas the set of the facets at 43.96, 51.41 and 75.68 is shifted to the metallic Cu (#00-004-0836) and may correspond to the Cu-rich Ni-Cu alloys.

Peer-reviewed version available at Catalysts 2018, 8, 454; doi:10.3390/catal8100454

Thus, chemical reduction of the inorganic precursors on carbon support using sodium borohydride as the reducing agent results in the formation of near-spherical nanoparticles with poor crystallinity and the average particle size of ca. 10 nm. In the binary Ni_3TM_1/C catalysts, heterogeneous co-distribution the metallic components was observed, with partially separated areas of Cu_2O in Ni_3Cu_1, and segregation of Ni on the surface for all the samples. Homogeneity of the metallic components co-distribution in the bulk of the as-synthesized catalysts and the separation of the XRD reflexes after the thermal treatment at 450 °C illustrates that the binary Ni_3TM_1/C catalysts are predominantly composites - mechanical mixtures of either Ni with TM, or mixture of several Ni_xTM_y alloys.

2.3. Electrochemical characterization

Figure 2 (a) shows the first several cycles of the HOR polarization curves (solid lines) on Ni/C catalyst and compares them with the corresponding cyclic voltammogram registered in Ar atmosphere (dash line). Opposed to the behavior of the TM-doped catalysts, bare Ni shows significant increase of the catalytic activity after the first HOR cycle (Figure 2, a), namely after the partial electrochemical oxidation of the surface. The positive effect of the surface pre-oxidation on the Ni catalytic activity in HOR was also reported previously [52,63]. This observation might serve as a direct experimental evidence of the bifunctional mechanism of HOR [26,50,64–67], when OH_{ad} species, pre-chemisorbed on the adjacent active sites, are required in order to remove H_{ad} chemisorbed on the free metallic surface of Ni, and to make the hydrogen oxidation reaction proceed. Thus, presumably a certain optimal ratio of $Ni(OH_{ad})/Ni(H_{ad})$ sites is needed to retain the HOR activity of bare Ni electrocatalyst. Therefore, the theoretical estimations of HBE and OHBE, provided in Figure 1, (a) and (b), might shed some light on the understanding of the competitive co-adsorption of H and OH species (see section 2.1). Noteworthy, Ni_3TM_1 catalysts do not require preliminary electrooxidation cycle, which might be related either to the fact that the presence of TMs with higher affinity to oxygen (such as Cu [68], Co [69] and Fe [69]) stabilizes the oxygenated species on the surface of Ni, or the TMs serve by themselves as the active sites for formation of OH_{ad} species. In any case, an important theoretical question arises: would a hypothetical surface with the optimal value of HBE (discussed earlier) and no affinity to chemisorption of OH species catalyze HOR in alkaline media? Might it be the case that PGMs (e.g. Pt, Ir, Rh) show two orders of magnitude lower catalytic activity in HOR in alkaline media compared to acidic one [45,49,56], because in the potential range of hydrogen electrooxidation the surfaces produce negligibly low ratio $PGM(H_{ad})/PGM(OH_{ad})$? The doping of PGMs by TMs with high affinity to chemisorption of OH species was shown to result in the HOR catalysis promotion [67,70,71]. However, this subject is beyond the scope of this work.

HOR polarization curves in the potential range of 0÷0.4 V, presented in Figures 3 (a) and (b), show electrocatalytic behavior of Ni/C, Ni_3Fe_1/C, Ni_3Co_1/C and Ni_3Cu_1/C typical for polycrystalline Ni [51], or TM doped Ni electrocatalysts [34]. For all the catalysts, during the forward scan (Figure 2, a and b), a peak of HOR is observed, with the current increasing up to certain potential values (see the peak potential values in Figure 2, b). Further, the surface deactivates with the increase of the potential due to the increasing surface electrooxidation, and at $E > 0.4$ V there is no catalytic activity in HOR. Similar effect was observed in HOR for Ru/C [72] due to the competitive adsorption of H_2 and OH^-. On the backward scan, the surface of the catalysts reactivates, due to the reversible electrochemical reduction of Ni (see black solid and dash circles marking the onset of HOR and Ni electroreduction, respectively, on the backward scans).

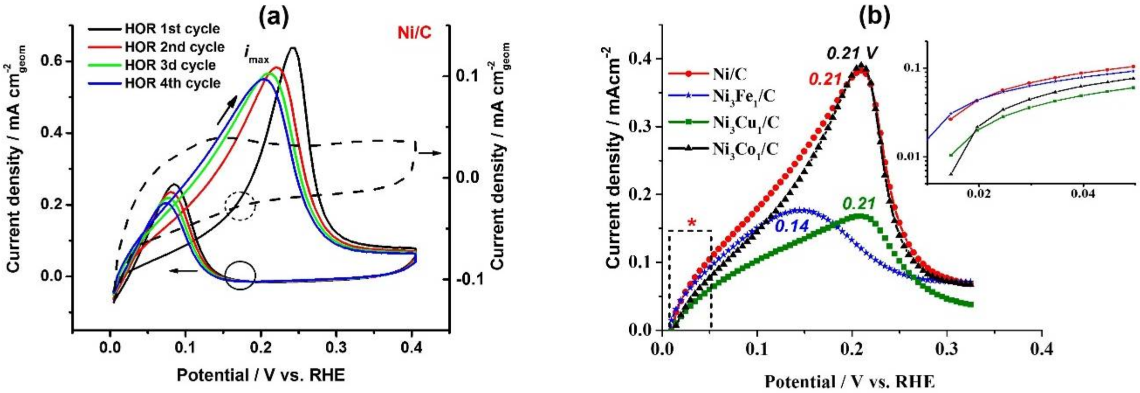

Figure 2. (a) HOR polarization curves (solid lines) and cyclic voltammogram (dash line) for the Ni/C catalyst. The arrows show the potential sweep direction. (b) Comparison of the HOR polarization curves (forward scans) for monometallic Ni/C and bimetallic Ni_3TM_1/C catalysts for TM = Fe, Co and Cu. The numbers correspond to the peak potential values. * - potential range of 0.01÷0.05 V used for the kinetic analysis.

The analysis of the HOR kinetics in the micropolarization area (0.01÷0.05 V) reveals clear effect of the dopant on the exchange current density: at the comparable values of ECSA, bare Ni/C shows 0.039 mA cm^{-2}_{Ni} (Table 1), whereas addition of Fe, for instance, results in significant reaction promotion with 0.06 mA cm^{-2}_{Ni}, which in turn positively effects mass specific activity, 1.6 A g^{-1}_{Ni} vs. 1.87 g^{-1}_{Ni} (Table 1). The i_0 values reported in this work exceed the highest i_0 values reported earlier in the literature, for instance, 0.028 mA cm^{-2}_{Ni} for hydrothermally synthesized 70 %Ni/N-CNT [28], or 0.027 mA cm^{-2}_{Ni} for thermally reduced 50% Ni_9Mo_1/C [34] and 0.025 mA cm^{-2}_{Ni} for 50% $Ni_{9.5}Cu_{0.5}/C$ [73], showing that chemical reduction might be a promising approach for the further development of Ni-based catalysts. However, overall catalyst mass activity of our catalysts is lower (0.35÷0.55 A g^{-1}_{cat}) for the binary electrocatalysts compared to the bare Ni/C (0.6 A g^{-1}_{cat}), due to the high concentration of the catalytically inert TMs. The mass catalytic values are lower (6.5 A g^{-1}_{cat} for 70 %Ni/N-CNT [28], 3.54 A g^{-1}_{cat} for the electrodeposited CoNiMo [29], 2.9 A g^{-1}_{cat} for 50% Ni_9Mo_1/C [34]) or comparable (0.94 A g^{-1}_{cat} for 25% $Ni_{9.5}Cu_{0.5}$/Vulcan XC72 [37]) to the published ones. In previous works, the authors have applied preliminary electrochemical reduction of the surface, which allowed increasing the surface area up to 10÷20 m² g^{-1}_{Ni}. In our work, we have intentionally avoided preliminary reduction step in order to demonstrate that carbon supported nanoparticles synthesized via simple chemical reduction method at ~0 °C can be handled in the ambient atmosphere, and they can still retain their electrocatalytic activity, opposed, for instance, to the thermally obtained Ni-based electrocatalysts [34].

Table 1. Comparison of surface area values and the HOR electrocatalytic properties for different catalysts.

Catalyst	ESCA / m² g^{-1}_{Ni}	i at η=0.05 V				i_0		
		mA cm^{-2}_{geom}	A g^{-1}_{cat}	A g^{-1}_{Ni}	A m^{-2}_{Ni}	A g^{-1}_{Ni}	mA cm^{-2}_{Ni}	
Ni/C	1.3 ± 0.2	0.12	0.6	1.60	0.347	0.83	0.039	+ 0.018 - 0.013
Ni_3Fe_1/C	1.2 ± 0.6	0.11	0.55	1.87	0.858	0.96	0.060	+ 0.008 - 0.008
Ni_3Cu_1/C	1.2 ± 0.2	0.09	0.45	2.01	0.510	0.98	0.051	+ 0.001 - 0.0012
Ni_3Co_1/C	1.5 ± 0.3	0.07	0.35	1.28	0.290	0.66	0.020	+ 0.030 - 0.003

Peer-reviewed version available at Catalysts 2018, 8, 454; doi:10.3390/catal8100454

Figures 3 (a-d) show the linear potential stripping (solid lines) for the catalysts under Ar atmosphere at the same potential sweep rate (1 mV s^{-1}) used to register the HOR polarization curves, and the corresponding derivatives of the HOR polarization curves (dash lines), for all the catalysts. The charge consumed for the full surface coverage by Ni(OH)$_2$ (the area under the solid line peaks,) was used to estimate the electrochemical surface area (ECSA) of Ni. The ECSA values are presented in Table 1. Extremely low ECSA values were obtained in all catalysts (< 2 m^2 g^{-1}_{Ni} compares to the expected ~ 70 m^2 g^{-1}_{Ni} based on TEM images, Figure S1, Supporting Information), which are probably due to the oxidative surface passivation evidenced by EDS (Table S1, Supporting Information) and XPS (Tables S1 and S3, Figure S8, Supporting Information).

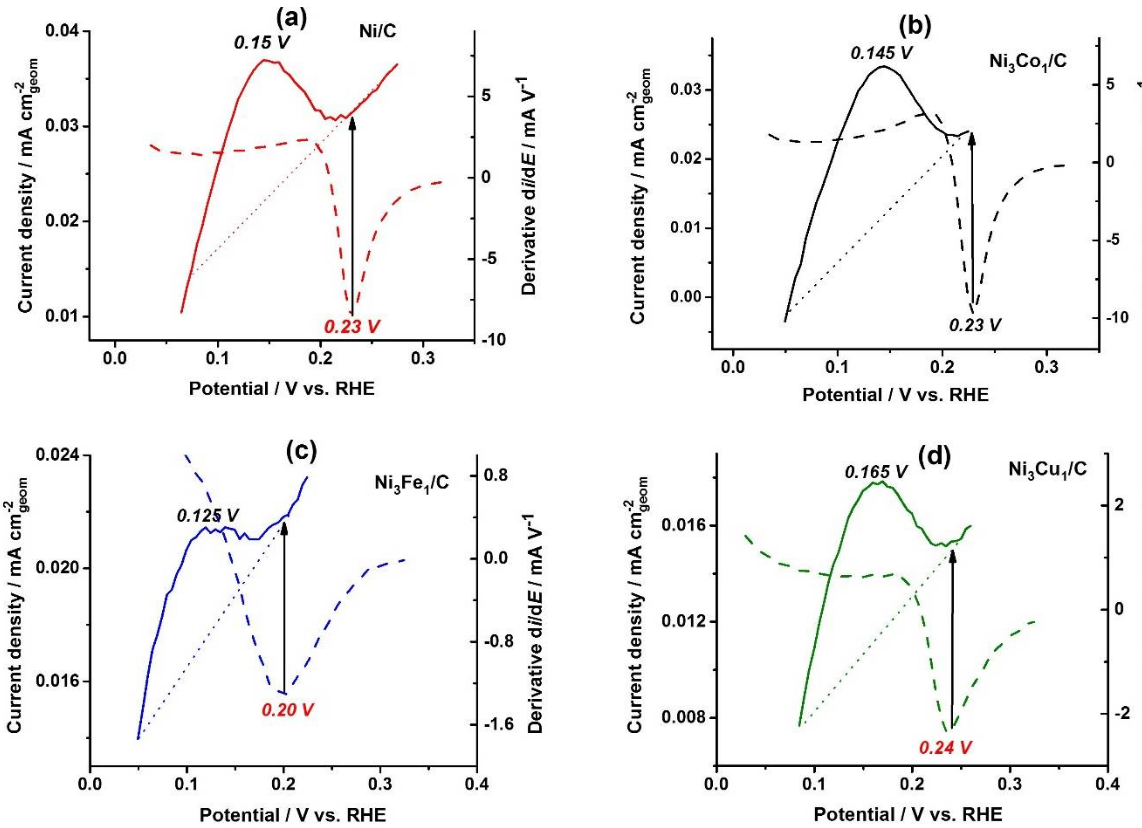

Figure 3. Linear potential stripping (solid lines) for the Ni/C (A), Ni$_3$Co$_1$/C (B), Ni$_3$Fe$_1$/C (C) and Ni$_3$Cu$_1$/C (D) catalysts under Ar atmosphere and the corresponding derivatives (dash lines) of the HOR polarization curves. Numbers indicate the peak potential values.

The HOR polarization curves (Figure 2, b) were differentiated, and the potential values corresponding to the minimum of the derivatives (dash lines, Figure 3, a-d) were used as one of the catalyst characteristic parameters, showing the potential of the catalytic activity loss. As seen from Figure 3, a-d, the potentials of the derivative minimum (marked in red: 0.23, 0.23, 0.20 and 0.24 V for on the bare Ni/C, Ni$_3$Co$_1$/C, Ni$_3$Fe$_1$/C and Ni$_3$Cu$_1$/C, respectively) correspond to the full surface coverage (indicated by black arrows). Full surface coverage by monolayer of Ni(OH)$_2$ on the bare Ni/C, Ni$_3$Co$_1$/C and Ni$_3$Cu$_1$/C takes place at more anodic potential (0.23 V, 0.23 and 0.24 V, respectively, Figure 3, a, b, d), whereas the surface of Ni$_3$Fe$_1$/C is fully covered already at 0.20 V (Figure 3, c). The peak potential of Ni$_3$Fe$_1$/C electrooxidation (solid line, Figure 3, c), 0.125 V, is negatively shifted as well compared to Ni/C (Figure 3, a), Ni$_3$Co$_1$/C (Figure 3, b) and Ni$_3$Cu$_1$/C (Figure 4, d). Thus, Ni-Fe catalysts are prone to the higher OH$_{ad}$ coverage at lower overpotentials, which results in higher HOR catalytic activity at lower overpotential values (Figure 3, B, insert).

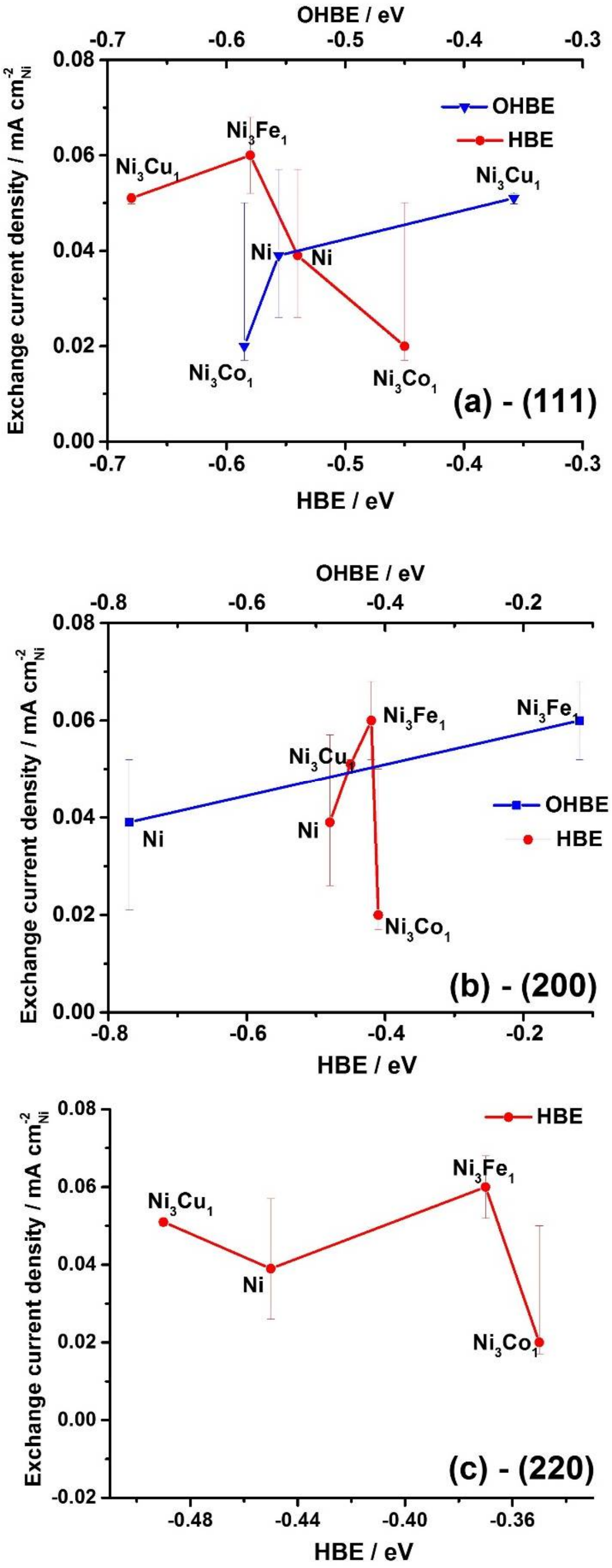

Figure 4. Correlation between the experimentally determined exchange current density values of the catalysts with the theoretically predicated HBE and OHBE values: a – (111) facet, b – (200) facet, and c – (220) facet.

Figure 4 (a) shows the general trend of decrease in exchange current density values with the increase of HBE value increase for the facet (111), whereas the opposite trend is expected (see section 2.1. Theoretical prediction). At the same time, the expected catalytic activity increase is observed with the increase of HBE for the facets (200) and (220) (Figure 4, b and c). This observation might indicate that the catalytic activity is predominantly determined by higher index surfaces, (200) and (220). Figures 5(A) and (B) also show that i_o increases as OHBE values increase. The latter observation might serve as an indirect evidence of the bifunctional mechanism of the HOR hypothesized earlier in different studies [25,26,64] explaining the promotion effect of the dopants on the HOR kinetics. According to this bifunctional mechanism, there is a need for more than the conventional HBE indicator to describe the HOR in alkaline [22] – the OHBE indicator may bring the missing parameter to clearly understand the HOR kinetics and mechanism.

This study provides an initial thought supported with some first data on HBE and OHBE, both as important parameters to describe the electrocatalytical activity of Ni-based catalysts towards HOR in alkaline. Further DFT calculations and experimental studies of specifically Ni-TM facets are needed to increase this understanding.

3. Materials and Methods

3.1. Computational details

Spin-polarized DFT calculations were performed with the Vienna Ab Initio Simulation Package (VASP) [74,75]. We use the Perdew–Burke–Ernzerhof (PBE) [76] of the general gradient approximation (GGA) exchange-correlation functional in all computational calculations. This functional describes well all the chosen transition metal alloys [77–80]. Projected augmented wave (PAW) potentials [81,82] represented frozen core electrons and nuclei for each atom. For the whole first row 3d TM, including Sc, Ti, V, Cr, Mn, Fe, Co, Ni, Cu and Zn atoms, the appropriate PAW potentials for inner shell electrons are replaced with Ar's electronic configuration. Kohn-Sham (KS) equations were solved with a plane-wave basis. Symmetry operations were imposed for a better description of the geometry. *k*-space integration was performed with the tetrahedron method with Blöchl corrections [82].

We used a *k*-mesh of 3×3×1 in the Monkhorst–Pack scheme and an energy cutoff of 400 eV for the plane-wave basis set. These *k*-grid's and energy cutoff's were converged to a total energy lower than 1 meV atom^{-1}. For all of the calculations, we relaxed the cells using convergence criteria of 10^{-5} eV for electronic iterations and of 0.01 eV Å^{-1} for ionic iterations. Geometrical relaxations took place with a conjugate gradient algorithm [83]. All slabs were separated from their periodic image by a minimum of 16 Å vacuum layers, which is converged the total energy up to 0.1 meV atom^{-1}.

The unit cells of the catalytic materials were built with 25% of TM (i.e. atomic ratio Ni:TM = 3:1), with a FCC structure. We considered three facets that have been experimentally observed in the XRD spectra (Figure S5-S6, Supporting Information) of the electrocatalysts: Ni_3TM_1 facets (111), (200), and (220). The (111) and (200) facets were modeled by five-layer slab, while the (220) facet needed seven layers to converge the calculated adsorption energies. The hydrogen and OH adsorbate coverage corresponds to a low coverage of 1/16 monolayer (ML) for (111) and 1/8 ML for (200) and (220) surfaces, with supercell size of 2×2×1 (see Figure 5). The adsorbed hydrogen atoms and the top three layers of the slab were fully relaxed during energy relaxation by selecting several initial hydrogen positions and performing geometry optimization, until forces on all atoms reached the convergence threshold of 0.01 eV Å^{-1}. The rest of the atoms in the slab were fixed on its bulk lattice configuration since adding more atoms gave the same hydrogen binding energies. The most stable H adsorption sites found for Ni_3Fe_1 were adopted and used for all the Ni_3TM_1 systems. All the optimized ground state structures of bare and adsorbed hydrogen surfaces of 1×1 primitive cells and 2×2×1 sized supercell are listed in the Supporting Information.

Peer-reviewed version available at Catalysts 2018, 8, 454; doi:10.3390/catal8100454

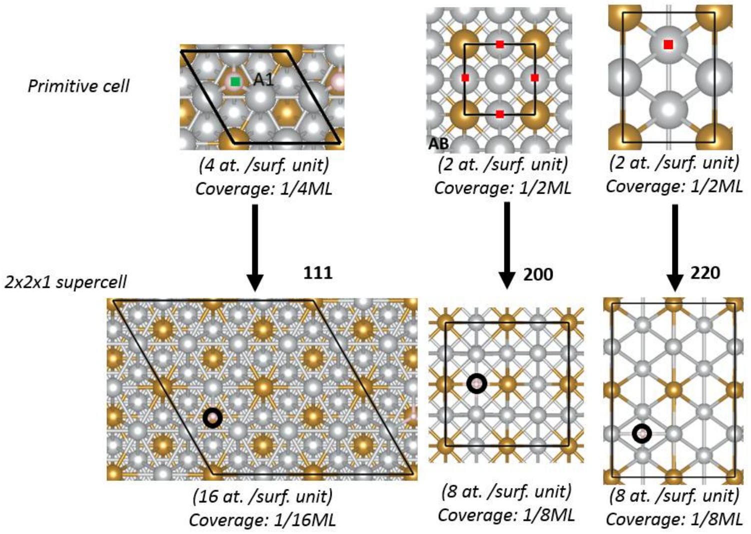

Figure 5: Slab models for all three Ni$_3$TM$_1$ (111), (200) and (220) facets constructed from the primitive cell. The locations marked by black circles indicate the H adsorption sites with the lowest energy.

3.2. Catalyst synthesis

Monometallic Ni/C and bimetallic Ni$_3$TM$_1$/C carbon-supported electrocatalysts were synthesized via chemical reduction method at 0 °C, using sodium borohydride as the reducing agent. To synthesize monometallic catalyst, 100 mg of VXCMAX22 (Cabot) carbon black, noted as C, was suspended in 15 ml of isopropanol (HPLC Plus GC, 99.9%, Sigma Aldrich) in the ultrasound bath (XUBA3, Grant Instruments) and then mixed with 15 ml aqueous solutions containing 1.7 mmol of $NiCl_2 \times 6H_2O$ (99.3%, Alfa Aesar). The mixture was cooled down in the ice-bath and deaerated by flowing Ar (99.999%, Maxima). For the synthesis of bimetallic Ni$_3$TM$_1$/C catalysts 15 ml of the solutions containing 0.567 mmol of either $FeCl_2 \times 4H_2O$ (99.95%, Sigma Aldrich), or $CoCl_2 \times 6H_2O$ (99.99%, Alfa Aesar), or $CuSO_4 \times 5H_2O$ (for analysis, Merck) were added to the carbon-$NiCl_2$ mixture. The intended weight ratio of nickel to carbon in monometallic Ni/C catalyst was 0.5-to-0.5. The same Ni-to-C weight ratio was kept for the bimetallic Ni$_3$TM$_1$/C catalysts, where the atomic ratio of Ni-to-TM was 3-to-1. Ice-cold solution containing 3.4 mmol of $NaBH_4$ (99.99%, Sigma Aldrich) in 25 ml of 0.1 M KOH (AR, BioLab) was used as the reducing agent. The reduction of the metal precursors was carried out in the ice bath by dropping $NaBH_4$ solution into the mixture while stirring. The precipitates were separated in the centrifuge (Eppendorf 5804). After being rinsed by milli-Q H_2O (18.2 MΩ×cm) five times at 10,000 rpm for 10 min, the samples were placed in the vacuum oven (1407-2, MRC) at r.t. and then dried at 80÷90 °C for 24 h. Before removing the samples from vacuum, the oven was cooled back to room temperature. The samples were stored in a desiccator under vacuum and handled in the ambient air.

3.3. Physical and chemical characterization

TEM images were obtained on FEI Tecnai T20 LaB$_6$ microscope operated at 200 kV. Catalyst powders were dispersed in isopropanol (2 mg$_{cat}$ per 10 ml) in ultrasound bath for 2 h, spray-casted onto a 300 mesh Cu grid coated with holey carbon (300 mesh, Agar Scientific), and then left to dry on the TEM grids at room temperature.

EDS spectra, STEM images and elemental mapping were collected on Zeiss Ultra-Plus HRSEM. EDS spectra were measured at accelerating voltages in the range of 5÷15 kV with the data collecting time 50÷150 s. STEM element mapping was done at 30 kV on holey carbon 200 mesh Cu TEM grids (Agar Scientific) with the applied catalysts.

XRD data were collected using Rigaku Smartlab diffractometer with Cu X-ray source (λ=1.5406 Å). XRD spectra were recorded in medium resolution parallel beam geometry at the tube current of 100 mA and tube voltage of 35 kV in θ/2θ scan mode with the scan rate of 1 deg. min^{-1} and step 0.01

Peer-reviewed version available at Catalysts 2018, 8, 454; doi:10.3390/catal8100454

deg. The structural data were compared to the ICSD database. Crystallite sizes were estimated using Scherrer's equation [84].

XPS measurements were performed in ultra-high 2.5×10^{-10} Torr base pressure) using 5600 Multi-Technique System (PHI, USA). The samples were irradiated with an AlK$_{\alpha}$ monochromated source (1486.6 eV) and the outcome electrons were analyzed by a Spherical Capacitor Analyzer using a slit aperture of 0.8 mm. Survey spectra were registered in a wide energy range (0÷1400 eV) at a low resolution. Utility multiplex spectra were taken for different peaks in a low energy range window at an intermediate (utility) resolution. Atomic concentration was calculated for all the elements present. Atomic concentration calculation accuracy was ±2, ±5, ±10 and ±20% for atomic concentrations around 50%, 20%, 5% and 1%, respectively.

3.4. Electrochemical characterization

Rotating disc electrode (RDE) method and cyclic voltammetry (CV) were applied to characterize the electrochemical properties of the catalysts using WaveDriver 20 Bipotentiostat/Galvanostat (Pine Research). For RDE tests, Nafion was used as only ionomer, to avoid surface adsorption effects of other ionomers onto the catalysts under study [85]. For these tests, 10 mg of the catalyst was suspended in 2 ml of isopropanol/water mixture (3/1 vol.). Nafion (10 wt.% in H_2O, ρ=1.05 g ml^{-1}, Sigma Aldrich) was added to the catalyst to get a Nafion:catalyst weight ratio of 0.15:1. The suspension was then drop-casted on glassy carbon disc (5.0 mm, PTFE shroud, Pine Research) to form a catalyst layer with a loading of 200 μg$_{cat}$ cm^{-2}. The electrode was dried in the air for an about 1 h and mounted on the rotating shaft. The experiments were conducted at 25 °C in 1 M KOH aqueous solution in a water-jacketed electrochemical cell. Pt wire (Pine Research) isolated in glass-fritted tube was used as the counter electrode. All the potential values were registered vs. Hg/HgO/1 M KOH (RE-61AP, ALS Co.).

Taking into account electrochemical properties of Ni, the following experimental protocol was elaborated using RDE and CV methods. Before immersing the working electrode into the electrolyte, it was purged by H_2 (electrolyzer SPH-500, H_2 purity 99.999%, H_2 flow 0÷500 ml min^{-1}, Jinan Mao An Instrument Co., Ltd) until the open circuit potential stabilized. The potential was then scanned repeatedly (up to 5 cycles) in the potential range between 0 V and 0.4 V vs. RHE, with the sweep rate of 1 mV s^{-1} and at a rotation speed of 1100 rpm, to register the HOR polarization curves. The values of exchange current density (i_0) were calculated in the micropolarization potential range applying equation (1) [50]:

$$i_0 \times (\alpha_c + \alpha_a) = \frac{RT}{F} \times \frac{i}{\eta} \qquad (1)$$

where α_a and α_c are the anodic and cathodic transfer coefficients, respectively, i is catalytic activity averaged for the range of overpotential values (η) between 5 to 50 mV (in A cm$^{-2}_{Ni}$), T is the temperature of the electrolyte (° K), R is the gas constant and F is the Faraday constant. Afterwards, the gas flow was changed to Ar until the open circuit potential was stabilized, and then the potential was swept in the potential range between 0 V and 0.4 V vs. RHE at the rate of 1 mV s^{-1}. The anodic peak is integrated and used as *in-situ* method to determine the electrochemical active surface area of Ni with the specific charge density of 514 μC cm$^{-2}_{Ni}$ [28].

4. Conclusions

Carbon supported nanoparticles of monometallic Ni catalyst and binary Ni-Transition Metal electrocatalytic composites were synthesized via chemical reduction method. Different TM dopants (Fe, Co and Cu) were studied in this work. The chemical composition, structure and morphology of the materials were characterized and related to the electrochemical properties towards HOR in alkaline medium. For the first time, both HBE and OHBE values were calculated for this kind of catalysts. DFT calculations showed the significant effect of the dopant TM onto the HBE and OHBE values of the different Ni-TM catalysts, which in turn affects their exchange current densities. It is proposed that both HBE and OHBE parameters will be used as the indicators of the electrocatalytic activity of Ni-TM catalysts towards a better understanding of these catalysts for the electrooxidation of hydrogen in alkaline medium.

Peer-reviewed version available at Catalysts 2018, 8, 454; doi:10.3390/catal8100454

A significant role of the dopant TM in the promotion of the hydrogen electrooxidation kinetics of the binary Ni-TM/C composites was revealed. A record-high in exchange current density value, 0.060 mA cm^2_{Ni}, was observed for Ni_3Fe_1/C. We therefore suggest that Ni-Fe/C could be a promising catalyst for HOR in alkaline media. Development of synthesis approaches and corresponding conditions to minimize surface oxidation of the metallic Ni in the Ni-TM/C materials may lead to the development of highly active HOR catalysts for PGM-free AEMFCs.

Supplementary Materials: The following are available online at www.mdpi.com/xxx/s1, Figure S1: title, Table S1: title, Video S1: title.

Author Contributions: Synthesis, electrochemical measurements, TEM, SEM, STEM, XRD, data analysis, writing and editing, E.D.S. Funding acquisition, supervision, review and editing, D.R.D. DFT HBE calculations, J.Z. DFT OHBE calculations, K.D. DFT supervision, DFT funding acquisition, review and editing – M.C.T.

Acknowledgments: This work was partially funded by the Nancy & Stephan Grand Technion Energy Program (GTEP); by the European Union's Horizon 2020 research and innovation program [grant No. 721065]; by the Ministry of Science, Technology & Space of Israel through the M.Era-NET Transnational Call 2015, NEXTGAME project [grant No. 3-12940] and through grant No. 3-12948; by the Israel Science Foundation (ISF) [grant No. 1481/17]; by the Russell Berrie Nanotechnology Institute, Technion; and by the Planning & Budgeting Committee / ISRAEL Council for Higher Education (CHE) and Fuel Choice Initiative (Prime Minister Office of ISRAEL), within the framework of “Israel National Research Center for Electrochemical Propulsion (INREP)”. This research was also partially carried out within the framework of the UConn-Technion Energy Collaboration initiative, supported by the Satell Family Foundation, the Maurice G. Gamze Endowed Fund (at the American Technion Society), Larry Pitt and Phillis Meloff, The Eileen and Jerry Lieberman UConn/Israel Global Partnership Fund and the Grand Technion Energy Program (GTEP).

Conflicts of Interest: The authors declare no conflict of interest.

Appendix A

Table A1. Ground state energies of bare metal/alloy and one with hydrogen at (111) facet (1/16 ML) supercell 2×2×1 and calculated HBE (all energies are in eVs).

Material	Bare (111) facet	Surface with Hydrogen	HBE / eV
Ni_3Sc_1	-465.27	-469.42	-0.77
Ni_3Ti_1	-498.92	-503.16	-0.86
Ni_3V_1	-500.72	-504.57	-0.47
Ni_3Cr_1	-496.02	-500.10	-0.70
Ni_3Mn_1	-494.24	-498.32	-0.69
Ni_3Fe_1	-479.68	-483.64	-0.58
Ni_3Co_1	-447.09	-450.93	-0.45
Ni bare	-414.05	-417.97	-0.54
Ni_3Cu_1	-380.83	-384.90	-0.68
Ni_3Zn_1	-344.05	-348.73	-1.29

Table A2. Ground state energies of bare and with hydrogen at (200) facet (1/8 ML) supercell 2×2×1 and calculated HBE (all energies are in eVs).

Material	Bare (200) facet	Surface with Hydrogen	HBE / eV
Ni_3Sc_1	-236.96	-240.79	-0.44
Ni_3Ti_1	-251.89	-255.84	-0.57
Ni_3V_1	-251.01	-254.94	-0.55
Ni_3Cr_1	-251.46	-255.31	-0.47
Ni_3Mn_1	-251.86	-255.78	-0.54
Ni_3Fe_1	-241.93	-245.73	-0.42
Ni_3Co_1	-222.10	-225.89	-0.41

Ni bare	-203.61	-207.47	-0.48
Ni_3Cu_1	-184.70	-188.53	-0.45
Ni_3Zn_1	-164.37	-167.95	-0.19

Table A3. Ground state energies of bare and with hydrogen at (220) facet (1/8 ML) supercell 2×2×1 and calculated HBE (all energies are in eVs).

Material	Bare (220) facet	Surface with Hydrogen	HBE / eV
Ni_3Sc_1	-328.56	-332.63	-0.69
Ni_3Ti_1	-349.00	-352.35	0.04
Ni_3V_1	-349.56	-353.17	-0.22
Ni_3Cr_1	-349.75	-353.55	-0.42
Ni_3Mn_1	-349.44	-353.30	-0.47
Ni_3Fe_1	-335.65	-339.40	-0.37
Ni_3Co_1	-309.08	-312.82	-0.35
Ni bare	-283.84	-287.67	-0.45
Ni_3Cu_1	-258.57	-262.44	-0.49
Ni_3Zn_1	-230.78	-234.80	-0.64

Table A4. Ground state energies of bare and with OH at (111) facet (1/16 ML) supercell 2×2×1 and calculated OHBE (all energies are in eVs).

Material	Bare (111) facet	Surface with OH	OHBE / eV
Ni_3Cr_1	-496.02	-506.77	-0.35
Ni_3Mn_1	-494.24	-504.68	-0.04
Ni_3Co_1	-447.09	-458.05	-0.57
Ni bare	-414.05	-424.99	-0.54
Ni_3Cu_1	-380.83	-391.58	-0.34

Table A5. Ground state energies of bare and with OH at (200) facet (1/8 ML) supercell 2×2×1 and calculated OHBE (all energies are in eVs).

Material	Bare (200) facet	Surface with OH	OHBE / eV
Ni_3Cr_1	-251.46	-263.04	-1.18
Ni_3Mn_1	-251.86	-263.06	-0.81
Ni_3Fe_1	-241.93	-252.45	-0.11
Ni bare	-203.61	-214.76	-0.75

Table A6. Ground state energies of bare and with OH at (220) facet (1/8 ML) supercell 2×2×1 and calculated OHBE (all energies are in eVs).

Material	Bare (220) facet	Surface with OH	OHBE / eV
Ni_3Cr_1	-349.75	-360.01	0.14
Ni_3Mn_1	-349.44	-360.01	-0.17
Ni_3Fe_1	-335.65	-345.11	0.93
Ni bare	-283.84	-294.73	-0.49

References

Peer-reviewed version available at *Catalysts* **2018**, *8*, 454; doi:10.3390/catal8100454

1. Varcoe, J. R.; Atanassov, P.; Dekel, D. R.; Herring, A. M.; Hickner, M. A.; Kohl, P. A.; Kucernak, A. R.; Mustain, W. E.; Nijmeijer, K.; Scott, K.; Xu, T.; Zhuang, L. Anion-exchange membranes in electrochemical energy systems. *Energy Environ. Sci.* **2014**, *7*, 3135–3191, doi:10.1039/b000000x.

2. Gottesfeld, S.; Dekel, D. R.; Page, M.; Bae, C.; Yan, Y.; Zelenay, P.; Kim, Y. S. Anion exchange membrane fuel cells: current status and remaining challenges. *J. Power Sources* **2018**, *375*, 170–184, doi:10.1016/j.jpowsour.2017.08.010.

3. Dekel, D. R.; Amar, M.; Willdorf, S.; Kosa, M.; Dhara, S.; Diesendruck, C. E. Effect of water on the stability of quaternary ammonium groups for anion exchange membrane fuel cell applications. *Chem. Mater.* **2017**, *29*, 4425–4431, doi:10.1021/acs.chemmater.7b00958.

4. Yim, S.-D.; Chung, H. T.; Chlistunoff, J.; Kim, D.-S.; Fujimoto, C.; Yang, T.-H.; Kim, Y. S. A Microelectrode study of interfacial reactions at the platinum-alkaline polymer interface. *J. Electrochem. Soc.* **2015**, *162*, F499–F506, doi:10.1149/2.0151506jes.

5. Dekel, D. R.; Willdorf, S.; Ash, U.; Amar, M.; Pusara, S.; Dhara, S.; Srebnik, S.; Diesendruck, C. E. The critical relation between chemical stability of cations and water in anion exchange membrane fuel cells environment. *J. Power Sources* **2018**, *375*, 351–360, doi:10.1016/j.jpowsour.2017.08.026.

6. Ziv, N.; Dekel, D. R. A practical method for measuring the true hydroxide conductivity of anion exchange membranes. *Electrochem. Commun.* **2018**, *88*, 109–113, doi:10.1016/j.elecom.2018.01.021.

7. Omasta, T. J.; Wang, L.; Peng, X.; Lewis, C. A.; Varcoe, J. R.; Mustain, W. E. Importance of balancing membrane and electrode water in anion exchange membrane fuel cells. *J. Power Sources* **2018**, *375*, 205–213, doi:10.1016/j.jpowsour.2017.05.006.

8. Diesendruck, C. E.; Dekel, D. R. Water – A key parameter in the stability of anion exchange membrane fuel cells. *Curr. Opin. Electrochem.* **2018**, *9*, 173–178, doi:10.1016/j.coelec.2018.03.019.

9. Zheng, Y.; Ash, U.; Pandey, R. P.; Ozioko, A. G.; Ponce-González, J.; Handl, M.; Weissbach, T.; Varcoe, J. R.; Holdcroft, S.; Liberatore, M. W.; Hiesgen, R.; Dekel, D. R. Water uptake study of anion exchange membranes. *Macromolecules* **2018**, *51*, 3264–3278, doi:10.1021/acs.macromol.8b00034.

10. Wang, L.; Bellini, M.; Miller, H. A.; Varcoe, J. R. A high conductivity ultrathin anion-exchange membrane with 500+ h alkali stability for use in alkaline membrane fuel cells that can achieve 2 W cm $^{-2}$ at 80 °C. *J. Mater. Chem. A* **2018**, *6*, 15404–15412, doi:10.1039/c8ta04783a.

11. Pusara, S.; Srebnik, S.; Dekel, D. R. Molecular simulation of quaternary ammonium solutions at low hydration levels. *J. Phys. Chem. C* **2018**, *122*, 11204–11213, doi:10.1021/acs.jpcc.8b00752.

12. Willdorf-Cohen, S.; Mondal, A.; Dekel, D. R.; Diesendruck, C. E. Chemical stability of

poly(phenylene oxide)-based ionomers in anion exchange-membrane fuel cell environment. *J. Mater. Chem. A* **2018**, doi:10.1039/c8ta05785k.

13. Krewer, U.; Weinzierl, C.; Ziv, N.; Dekel, D. R. Impact of carbonation processes in anion exchange membrane fuel cells. *Electrochim. Acta* **2018**, 263, 433–446, doi:10.1016/j.electacta.2017.12.093.

14. Ziv, N.; Mustain, W. E.; Dekel, D. R. The Effect of ambient carbon dioxide on anion-exchange membrane fuel cells. *ChemSusChem* **2018**, *11*, 1136–1150, doi:10.1002/cssc.201702330.

15. Ziv, N.; Mondal, A. N.; Weissbach, T.; Holdcroft, S.; Dekel, R. D. Effect of CO_2 on the properties of anion exchange membranes for fuel cell applications. *Macromolecules* (submitted).

16. Gerhardt, M. R.; Pant, L. M.; Weber, A. Z. Modeling water management and carbon dioxide contamination effects in anion-exchange membrane fuel cells. *Meet. Abstr.* **2018**, *MA2018-01*, 1752–1752.

17. Rasin, I. G.; Page, M.; Dekel, D. R.; Brandon, S. A model based analysis of alkaline membrane fuel cells. *ECS Trans.* **2017**, *80*, 1051–1057, doi:10.1149/08008.1051ecst.

18. Dekel, D. R.; Rasin, I. G.; Page, M.; Brandon, S. Steady state and transient simulation of anion exchange membrane fuel cells. *J. Power Sources* **2018**, *375*, 191–204, doi.org/10.1016/j.jpowsour.2017.07.012.

19. Dario R. Dekel, D.R.; Rasin, I. G.; Brandon, S. Predicting performance stability in anion exchange membrane fuel cells. *ACS Energy Lett.* (submitted).

20. Lefèvre, M.; Proietti, E.; Jaouen, F.; Dodelet, J.-P. Iron-based catalysts with improved oxygen reduction activity in polymer electrolyte fuel cells. *Science* **2009**, *324*, 71–74, doi:10.1126/science.1170051.

21. Bashyam, R.; Zelenay, P. A class of non-precious metal composite catalysts for fuel cells. *Nature* **2006**, *443*, 63–66, doi:10.1038/nature05118.

22. Davydova, E. S.; Mukerjee, S.; Jaouen, F.; Dekel, D. R. Electrocatalysts for hydrogen oxidation reaction in alkaline electrolytes. *ACS Catal* **2018**, 8, 6665-6690, doi:10.1021/acscatal.8b00689.

23. Wang, L.; Magliocca, E.; Cunningham, E. L.; Mustain, W. E.; Poynton, S. D.; Escudero-Cid, R.; Nasef, M. M.; Ponce-González, J.; Bance-Souahli, R.; Slade, R. C. T.; Whelligan, D. K.; Varcoe, J. R. An optimised synthesis of high performance radiation-grafted anion-exchange membranes. *Green Chem.* **2017**, *19*, 831–843, doi:10.1039/c6gc02526a.

24. Dekel, D. R. Review of cell performance in anion exchange membrane fuel cells. *J. Power Sources* **2018**, *375*, 158–169, doi:10.1016/j.jpowsour.2017.07.117.

25. Miller, H. A.; Vizza, F.; Marelli, M.; Zadick, A.; Dubau, L.; Chatenet, M.; Geiger, S.; Cherevko,

S.; Doan, H.; Pavlicek, R. K.; Mukerjee, S.; Dekel, D. R. Highly active nanostructured palladium-ceria electrocatalysts for the hydrogen oxidation reaction in alkaline medium. *Nano Energy* **2017**, *33*, 293–305, doi:10.1016/j.nanoen.2017.01.051.

26. Alesker, M.; Page, M.; Shviro, M.; Paska, Y.; Gershinsky, G.; Dekel, D. R.; Zitoun, D. Palladium/nickel bifunctional electrocatalyst for hydrogen oxidation reaction in alkaline membrane fuel cell. *J. Power Sources* **2016**, *304*, 332–339, doi:10.1016/j.jpowsour.2015.11.026.

27. Omasta, T. J.; Peng, X.; Miller, H. A.; Vizza, F.; Wang, L.; Varcoe, J. R.; Dekel, D. R.; Mustain, W. E. Beyond 1.0 W cm $^{-2}$ performance without platinum: the beginning of a new era in anion exchange membrane fuel cells. *J. Electrochem. Soc.* **2018**, *165*, J3039–J3044, doi:10.1149/2.0071815jes.

28. Zhuang, Z.; Giles, S. A.; Zheng, J.; Jenness, G. R.; Caratzoulas, S.; Vlachos, D. G.; Yan, Y. Nickel supported on nitrogen-doped carbon nanotubes as hydrogen oxidation reaction catalyst in alkaline electrolyte. *Nat. Commun.* **2016**, *7*, 1–8, doi:10.1038/ncomms10141.

29. Sheng, W.; Bivens, A. P.; Myint, M.; Zhuang, Z.; Forest, R. V.; Fang, Q.; Chen, J. G.; Yan, Y. Non-precious metal electrocatalysts with high activity for hydrogen oxidation reaction in alkaline electrolytes. *Energy Environ. Sci.* **2014**, *7*, 1719–1724, doi:10.1039/c3ee43899f.

30. Kristinsdóttir, L.; Skúlason, E. A systematic DFT study of hydrogen diffusion on transition metal surfaces. *Surf. Sci.* **2012**, *606*, 1400–1404, doi:10.1016/j.susc.2012.04.028.

31. Lu, S. F.; Pan, J.; Huang, A. B.; Zhuang, L.; Lu, J. T. Alkaline polymer electrolyte fuel cells completely free from noble metal catalysts. *Proc. Natl. Acad. Sci. U. S. A.* **2008**, *105*, 20611–20614, doi:10.1073/pnas.0810041106.

32. Mauer, A. E.; Kirk, D. W.; Thorpe, S. J. The role of iron in the prevention of nickel electrode deactivation in alkaline electrolysis. *Electrochim. Acta* **2007**, *52*, 3505–3509, doi:10.1016/j.electacta.2006.10.037.

33. Bates, M. K.; Jia, Q.; Ramaswamy, N.; Allen, R. J.; Mukerjee, S. Composite Ni/NiO-Cr_2O_3 catalyst for alkaline hydrogen evolution reaction. *J. Phys. Chem. C* **2015**, *119*, 5467–5477, doi:10.1021/jp512311c.

34. Kabir, S. A.; Lemire, K.; Artyushkova, K.; Roy, A.; Odgaard, M.; Schlueter, D.; Oshchepkov, A.; Bonnefont, A.; Savinova, E.; Sabarirajan, D. C.; Mandal, P.; Crumlin, E. J.; Zenyuk, I. V; Atanassov, P.; Serov, A. Platinum group metal-free NiMo hydrogen oxidation catalysts: high performance and durability in alkaline exchange membrane fuel cells. *J. Mater. Chem. A* **2017**, *5*, 24433–24443, doi:10.1039/c7ta08718g.

35. Oshchepkov, A.; Simonov, P.; Cherstiouk, O.; Nazmutdinov, R.; Glukhov, D.; Zaikovskii, V.; Kardash, T.; Kvon, R.; Bonnefont, A.; Simonov, A.; Parmon, V.; Savinova, E. On the effect of Cu on the Activity of carbon supported Ni nanoparticles for hydrogen electrode reactions in alkaline medium. *Top. Catal.* **2015**, *58*, 1–12, doi:10.1007/s11244-015-0487-5.

Peer-reviewed version available at *Catalysts* **2018**, *8*, 454; doi:10.3390/catal8100454

36. Tang, M. H.; Hahn, C.; Klobuchar, A. J.; Ng, J. W. D.; Wellendorff, J.; Bligaard, T.; Jaramillo, T. F. Nickel–silver alloy electrocatalysts for hydrogen evolution and oxidation in an alkaline electrolyte. *Phys. Chem. Chem. Phys.* **2014**, *16*, 19250–19257, doi:10.1039/c4cp01385a.

37. Cherstiouk, O. V.; Simonov, P. A.; Oshchepkov, A. G.; Zaikovskii, V. I.; Kardash, T. Y.; Bonnefont, A.; Parmon, V. N.; Savinova, E. R. Electrocatalysis of the hydrogen oxidation reaction on carbon-supported bimetallic NiCu particles prepared by an improved wet chemical synthesis. *J. Electroanal. Chem.* **2016**, *783*, 146–151, doi:10.1016/j.jelechem.2016.11.031.

38. Davydova, E. S.; Dekel, D. R. Ni-Based Hydrogen Oxidation reaction electrocatalysts for alkaline anion-exchange membrane fuel cells: systematic study on the doping effect. *Meet. Abstr.* **2017**, *MA2017-02*, 1635–1635.

39. Sheng, W.; Zhuang, Z.; Gao, M.; Zheng, J.; Chen, J. G.; Yan, Y. Correlating hydrogen oxidation and evolution activity on platinum at different pH with measured hydrogen binding energy. *Nat. Commun.* **2015**, *6*, 1–6, doi:10.1038/ncomms6848.

40. Zheng, J.; Zhuang, Z.; Xu, B.; Yan, Y. Correlating hydrogen oxidation/evolution reaction activity with the minority weak hydrogen-binding sites on Ir/C catalysts. *ACS Catal.* **2015**, *5*, 4449–4455, doi:10.1021/acscatal.5b00247.

41. Nørskov, J. K.; Bligaard, T.; Logadottir, A.; Kitchin, J. R.; Chen, J. G.; Pandelov, S.; Stimming, U. Trends in the exchange current for hydrogen evolution. *J. Electrochem. Soc.* **2005**, *152*, J23–J26, doi:10.1149/1.1856988.

42. Erdey-Gruz, T.; Volmer, M. Zur Theorie der Wasserstoff Überspannung. *Z. Phys. Chem. Abteil. Chem. Thermodyn. Kinet. Electrochem. Eig.* **1930**, *150*, 203–206.

43. Heyrovsky, J. A theory of overpotential. *Recl. des Trav. Chim. des Pays-Bas* **1927**, *46*, 582–585, doi:10.1002/recl.19270460805.

44. Marković, N. M.; Sarraf, S. T.; Gasteiger, H. A.; Ross, P. N. Hydrogen electrochemistry on platinum low-index single-crystal surfaces in alkaline solution. *J. Chem. Soc., Faraday Trans.* **1996**, *92*, 3719–3725, doi:10.1039/FT9969203719.

45. Sheng, W.; Gasteiger, H. A.; Shao-Horn, Y. Hydrogen oxidation and evolution reaction kinetics on platinum: acid vs alkaline electrolytes. *J. Electrochem. Soc.* **2010**, *157*, B1529, doi:10.1149/1.3483106.

46. Ross, P. N.; Stonehart, P. Correlations between electrochemical activity and heterogeneous catalysis for hydrogen dissociation on platinum. *J. Res. Inst. Catal. Hokkaido Univ.* **1974**, *22*, 22–41.

47. Bagotzky, V. S.; Osetrova, N. V. Investigations of hydrogen ionization on platinum with the help of micro-electrodes. *J. Electroanal. Chem.* **1973**, *43*, 233–249, doi:10.1016/S0022-0728(73)80494-2.

48. Stonehart, P.; Kohlmayr, G. Effect of poisons on kinetic parameters for platinum electrocatalyst sites. *Electrochim. Acta* **1972**, *17*, 369–382, doi:10.1016/0013-4686(72)80035-5.

49. Zheng, J.; Sheng, W.; Zhuang, Z.; Xu, B.; Yan, Y. Universal dependence of hydrogen oxidation and evolution reaction activity of platinum-group metals on pH and hydrogen binding energy. *Sci. Adv.* **2016**, *2*, e1501602 (1-8), doi:10.1126/sciadv.1501602.

50. Durst, J.; Siebel, A.; Simon, C.; Hasche, F.; Herranz, J.; Gasteiger, H. A. a New insights into the electrochemical hydrogen oxidation and evolution reaction mechanism. *Energy Environ. Sci.* **2014**, *7*, 2255–2260, doi:10.1039/c4ee00440j.

51. Floner, D.; Lamy, C.; Leger, J. M. Electrocatalytic oxidation of hydrogen on polycrystal and single-crystal nickel electrodes. *Surf. Sci.* **1990**, *234*, 87–97, doi:10.1016/0039-6028(90)90668-X.

52. Oshchepkov, A. G.; Bonnefont, A.; Saveleva, V. A.; Papaefthimiou, V.; Zafeiratos, S.; Pronkin, S. N.; Parmon, V. N.; Savinova, E. R. Exploring the influence of the nickel oxide species on the kinetics of hydrogen electrode reactions in alkaline media. *Top. Catal.* **2016**, *59*, 1319–1331, doi:10.1007/s11244-016-0657-0.

53. Schmidt, T. J.; Ross, P. N.; Markovic, N. M. Temperature dependent surface electrochemistry on Pt single crystals in alkaline electrolytes: Part 2. The hydrogen evolution/oxidation reaction. *J. Electroanal. Chem.* **2002**, *524*, 252–260, doi:10.1016/S0022-0728(02)00683-6.

54. Mahoney, E. G.; Sheng, W.; Yan, Y.; Chen, J. G. Platinum-modified gold electrocatalysts for the hydrogen oxidation reaction in alkaline electrolytes. *ChemElectroChem* **2014**, *1*, 2058–2063, doi:10.1002/celc.201402159.

55. Alia, S. M.; Pivovar, B. S.; Yan, Y. Platinum coated copper nanowires with high activity for hydrogen oxidation reaction in base. *J. Am. Chem. Soc.* **2013**, *135*, 13473–13478, doi:10.1021/ja405598a.

56. Elbert, K.; Hu, J.; Ma, Z.; Zhang, Y.; Chen, G.; An, W.; Liu, P.; Isaacs, H. S.; Adzic, R. R.; Wang, J. X. Elucidating hydrogen oxidation/evolution kinetics in base and acid by enhanced activities at the optimized pt shell thickness on the ru core. *ACS Catal.* **2015**, *5*, 6764–6772, doi:10.1021/acscatal.5b01670.

57. Balzarotti, A.; De Crescenzi, M.; Motta, N.; Patella, F.; Sgarlata, A. Valence charge fluctuations in $YBa_2Cu_3O_{7-\delta}$ from core-level spectroscopies. *Phys. Rev. B* **1988**, *38*, 6461–6469, doi:10.1103/PhysRevB.38.6461.

58. Mansour, A. N. Copper MgK_α XPS spectra from the physical electronics model 5400 spectrometer. *Surf. Sci. Spectra* **1994**, *3*, 202–210, doi:10.1116/1.1247748.

59. Jolley, J. G.; Geesey, G. G.; Hankins, M. R.; Wright, R. B.; Wichlacz, P. L. Auger electron and X-ray photoelectron spectroscopic study of the biocorrosion of copper by alginic acid polysaccharide. *Appl. Surf. Sci.* **1989**, *37*, 469–480, doi:10.1016/0169-4332(89)90505-9.

Peer-reviewed version available at *Catalysts* **2018**, *8*, 454; doi:10.3390/catal8100454

60. Hussain, Z.; Salim, M. A.; Khan, M. A.; Khawaja, E. E. X-ray photoelectron and auger spectroscopy study of copper-sodium-germanate glasses. *J. Non. Cryst. Solids* **1989**, *110*, 44–52, doi:10.1016/0022-3093(89)90180-4.

61. Shabanova, I. N.; Trapeznikov, V. A. A study of the electronic structure of Fe_3C, Fe_3Al and Fe_3Si by X-ray photoelectron spectroscopy. *J. Electron Spectros. Relat. Phenomena* **1975**, *6*, 297–307, doi:10.1016/0368-2048(75)80039-9.

62. Tan, B. J.; Klabunde, K. J.; Sherwood, P. M. A. X-ray photoelectron spectroscopy studies of solvated metal atom dispersed catalysts. Monometallic iron and bimetallic iron-cobalt particles on alumina. *Chem. Mater.* **1990**, *2*, 186–191, doi:10.1021/cm00008a021.

63. Oshchepkov, A. G.; Bonnefont, A.; Parmon, V. N.; Savinova, E. R. On the effect of temperature and surface oxidation on the kinetics of hydrogen electrode reactions on nickel in alkaline media. *Electrochim. Acta* **2018**, *269*, 111–118, doi:10.1016/j.electacta.2018.02.106.

64. Miller, H. A.; Lavacchi, A.; Vizza, F.; Marelli, M.; Di Benedetto, F.; D'Acapito, F.; Paska, Y.; Page, M.; Dekel, D. R. A Pd/C-CeO_2 Anode Catalyst for high-performance platinum-free anion exchange membrane fuel cells. *Angew. Chem. Int. Ed. Engl.* **2016**, *55*, 6004–6007, doi:10.1002/anie.201600647.

65. Li, J.; Ghoshal, S.; Bates, M. K.; Miller, T. E.; Davies, V.; Stavitski, E.; Attenkofer, K.; Mukerjee, S.; Ma, Z.-F.; Jia, Q. Experimental proof of the bifunctional mechanism for the hydrogen oxidation in alkaline media. *Angew. Chemie Int. Ed.* **2017**, *56*, 15594–15598, doi:10.1002/anie.201708484.

66. Strmcnik, D.; Uchimura, M.; Wang, C.; Subbaraman, R.; Danilovic, N.; van der Vliet, D.; Paulikas, A. P.; Stamenkovic, V. R.; Markovic, N. M. Improving the hydrogen oxidation reaction rate by promotion of hydroxyl adsorption. *Nat. Chem.* **2013**, *5*, 300–306, doi:10.1038/nchem.1574.

67. Ramaswamy, N.; Ghoshal, S.; Bates, M. K.; Jia, Q.; Li, J.; Mukerjee, S. Hydrogen oxidation reaction in alkaline media: Relationship between electrocatalysis and electrochemical double-layer structure. *Nano Energy* 2017, *41*, 765–771, doi.org/10.1016/j.nanoen.2017.07.053.

68. Koper, M. T. M.; Van Santen, R. A. *Interaction of H, O and OH with metal surfaces*; 1999; Vol. 472.

69. Medford, A. J.; Vojvodic, A.; Hummelshøj, J. S.; Voss, J.; Abild-Pedersen, F.; Studt, F.; Bligaard, T.; Nilsson, A.; Nørskov, J. K. From the Sabatier principle to a predictive theory of transition-metal heterogeneous catalysis. *J. Catal.* **2015**, *328*, 36–42, doi:10.1016/j.jcat.2014.12.033.

70. Striebel, K. A.; McLarnon, F. R.; Cairns, E. J. Oxygen reduction on Pt in aqueous K_2CO_3 and KOH. *J. Electrochem. Soc.* **1990**, *137*, 3351–3359, doi:10.1149/1.2086221.

71. Wang, Y.; Wang, G.; Li, G.; Huang, B.; Pan, J.; Liu, Q.; Han, J.; Xiao, L.; Lu, J.; Zhuang, L. Pt–Ru catalyzed hydrogen oxidation in alkaline media: oxophilic effect or electronic effect?

Energy Environ. Sci. **2015**, *8*, 177–181, doi:10.1039/c4ee02564d.

72. Ohyama, J.; Sato, T.; Yamamoto, Y.; Arai, S.; Satsuma, A. Size specifically high activity of Ru nanoparticles for hydrogen oxidation reaction in alkaline electrolyte. *J. Am. Chem. Soc.* **2013**, *135*, 8016–8021, doi:10.1021/ja4021638.

73. Roy, A.; Talarposhti, M. R.; Normile, S. J.; Zenyuk, I. V.; De Andrade, V.; Artyushkova, K.; Serov, A.; Atanassov, P. Nickel–copper supported on a carbon black hydrogen oxidation catalyst integrated into an anion-exchange membrane fuel cell. *Sustain. Energy Fuels* **2018**, doi:10.1039/c8se00261d.

74. Kresse, G.; Hafner, J. Ab initio molecular dynamics for open-shell transition metals. *Phys. Rev. B* **1993**, *48*, 13115–13118, doi:10.1103/PhysRevB.48.13115.

75. Kresse, G.; Furthmüller, J. Efficiency of ab-initio total energy calculations for metals and semiconductors using a plane-wave basis set. *Comput. Mater. Sci.* **1996**, *6*, 15–50, doi:10.1016/0927-0256(96)00008-0.

76. Perdew, J. P.; Burke, K.; Ernzerhof, M. Generalized gradient approximation made simple. *Phys. Rev. Lett.* **1996**, *77*, 3865–3868, doi:10.1103/PhysRevLett.77.3865.

77. Stamenkovic, V. R.; Fowler, B.; Mun, B. S.; Wang, G.; Ross, P. N.; Lucas, C. A.; Markovic, N. M. Improved oxygen reduction activity on $Pt_3Ni(111)$ via Increased surface site availability. *Science* **2007**, *315*, 493–497, doi:10.1126/science.1135941.

78. Studt, F.; Abild-Pedersen, F.; Bligaard, T.; Sorensen, R. Z.; Christensen, C. H.; Norskov, J. K. Identification of non-precious metal alloy catalysts for selective hydrogenation of acetylene. *Science* **2008**, *320*, 1320–1322, doi:10.1126/science.1156660.

79. Nikolla, E.; Schwank, J.; Linic, S. Comparative study of the kinetics of methane steam reforming on supported Ni and Sn/Ni alloy catalysts: The impact of the formation of Ni alloy on chemistry. *J. Catal.* **2009**, *263*, 220–227, doi.org/10.1016/j.jcat.2009.02.006.

80. Sitthisa, S.; An, W.; Resasco, D. E. Selective conversion of furfural to methylfuran over silica-supported NiFe bimetallic catalysts. *J. Catal.* **2011**, *284*, 90–101, doi.org/10.1016/j.jcat.2011.09.005.

81. Kresse, G. From ultrasoft pseudopotentials to the projector augmented-wave method. *Phys. Rev. B* **1999**, *59*, 1758–1775, doi:10.1103/PhysRevB.59.1758.

82. Blöchl, P. E. Projector augmented-wave method. *Phys. Rev. B* **1994**, *50*, 17953–17979, doi:10.1103/PhysRevB.50.17953.

83. Ziegel, E.; Press, W.; Flannery, B.; Teukolsky, S.; Vetterling, W. Numerical recipes: the art of scientific computing. *Technometrics* **1987**, doi:10.2307/1269484.

84. Patterson, A. L. The Scherrer formula for X-ray particle size determination. *Phys. Rev.* **1939**,

56, 978–982, doi:10.1103/PhysRev.56.978.

85. Maurya, S.; Dumont, J.; Narvaez Villarrubia, C.; Matanovic, I.; Li, D.; Kim, Y. S.; Noh, S.; Han, J.; Bae, C.; Miller, H. A.; Fujimoto, C. H.; Dekel, D. R. Surface adsorption affects the performance of alkaline anion-exchange membrane fuel cells. *ACS Catal.* **2018**, 8, 9429–9439, doi:10.1021/acscatal.8b03227.